Domestic induction heating system with standard primary inductor for reduced-size and high distance cookware

Emilio Plumed, *Student,Member, IEEE* (iD)*,* Ignacio Lope, *Member, IEEE* (iD)*,* Jesús Acero, *Senior, Member, IEEE* (iD)*,* and José Miguel Burdío, *Senior, Member, IEEE* (iD)

Abstract—In this work, a hybrid wireless power transfer system which combines induction heating (IH) and inductive power transfer (IPT) functionalities is proposed to improve the performance of a domestic induction heating application with small loads weakly coupled to distant inductors. Considering the basic single-inductor domestic IH application, the addition of a secondary inductor with series compensation capacitor directly attached to the small ferromagnetic cookware. This inductor allows to adapt the primary inductor to the load size, extending load distance while avoiding increased power losses and stress in electronic components. The extended distance can be used to implement the glassless induction concept, where the ceramic glass of typical cooktops is substituted by the kitchen surface itself. The design of the secondary coil is carried out by means of a combination of Finite Element simulations and electrical simulations. A design process including the housing of the resonant capacitors and the selection of the secondary winding number of turns and cabling is presented. As a result, a prototype is implemented and tested under working conditions up to 1500 W at several distances. Experimental results validate the electrical modelling and simulation. Moreover, thermal results confirm the feasibility of the proposal and validate the adopted strategies for the capacitor housing.

Index Terms—Induction Heating, Inductive Coupling, Home Appliances, Finite Element Method, Electromagnetic Analysis.

I. INTRODUCTION

Induction heating (IH) is the leading cooking technology in many countries because it provides an attractive set of features in comparison with traditional heating mechanisms. IH technology advantages mainly derive from its wireless nature, where the heat is directly generated in the load without any thermal energy transmitter [1]–[5]. As occurs in IPT arrangements, planar coils driven by an alternating current are in the heart of typical IH applications. This common element is fostering the development of new applications which share both IPT and IH characteristics [6].

Current tendencies in the domestic induction heating field move towards the integration of inductor coils under the

kitchen table, eliminating the cooktop, and resulting in versatile and unobstructed working surfaces where the available space for preparing dishes is extended, as well as facilitating easier cleaning [7]. However, this tendency involves several changes in the IH standard geometry which significatively modify the operation range. Typical IH applications have a distance between inductor and cookware (i.e. the load) of only 4 to 6 mm, which is determined by the thickness of the vitroceramic glass and other auxiliary elements. This distance ensure high efficiency and high power factor (PF) of the inductor-cookware coupled system [8]. However, as the inductor-load distance increases, in glassless applications to $10 - 40$ mm depending on the surface thickness, both efficiency and PF significatively decrease. Moreover, IH appliances must be able to heat vessels of small size, whose detection by the appliance is hampered by the height increase and consequent PF reduction. Traditionally, specific reduced-size inductors have been designed for this purpose [9], [10]. However, the distance increase between inductor and load in cooktop-integrated applications significatively damages the performance of small inductors [7]. Several commercial arrangements minimize this distance by drilling blind holes beneath the kitchen table, reducing its structural integrity.

The solution proposed in this work is inspired in IPT systems and preserves the worktop integrity. It consists of attaching a matching secondary inductor to the load, leaving the surface intact and working at high distance with high efficiency [11], [12], enabling the use of small sized loads. The combination of a primary and secondary inductors results in a system very similar to wireless power transfer [13]–[15]. However, the presence of the dissipative ferromagnetic load makes it a hybrid application which sometimes is called as inductively coupled heating system (ICH). In an ICH system the current fed to the primary inductor generates an electromagnetic field which simultaneously heats up the vessel and induces a current in the secondary inductor, which in turn generates its own electromagnetic field that heats up the load [11], [16]–[18]. Total transferred power depends on the amplitude and phase of both currents and therefore also depends on the compensation capacitors, the number of turns of the coils, the geometry (including the distance between the transmitter coil and the load, the transmitter diameter and the load diameter), the operating frequency and the physical properties of the load [19], [20]. Moreover, any manufacturing-oriented development should also consider efficiency and user

Fig. 1: Representation of the proposed glassless induction concept

Fig. 2: Representation of the proposed glassless induction concept

Fig. 3: System circuits: (a) Full system (b) Equivalent impedance
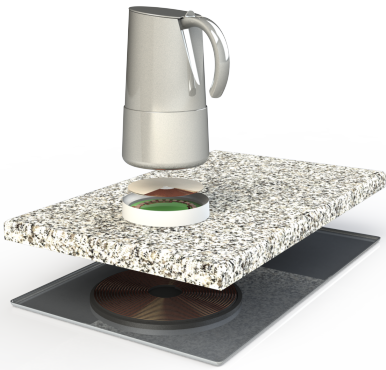
safety. The above considerations make the design of ICH systems difficult.

The design process of an ICH system involves several steps. Finite Element Analysis (FEA) tools are used to extract an electrical model of the ICH system dependent of the geometry and materials [21]. Spice-like simulations are carried out with the electrical model in order to evaluate different power electronics converters, compensation capacitors or pole splitting phenomenon. This methodology has been applied in previous designs [12], [16] where the focus mainly lay on the electrical modelling, reached power, power factor or temperature distribution. However, in the literature less attention has been paid to other aspects as the coil cabling selection or the location of the secondary compensation capacitor, which in general can be immersed in a strong varying magnetic field.

This paper describes the design, implementation and testing of an ICH capable of deliver up to $1500\,\mathrm{W}$ from a primary of diameter $\varnothing_{w1,\mathrm{ext}} = 180\,\mathrm{mm}$ to a small load of diameter $\varnothing_{\mathrm{load}} = \varnothing_{w1,\mathrm{ext}}/2 = 90\,\mathrm{mm}$ separated a distance up to $d_{\omega 1l} = 40\,\mathrm{mm}$. The transmitter size is standard in commercial IH cooktops and therefore the proposed design is compatible with existing products. It is worth pointing out that the mentioned power and load diameter entails a $23.6\,\mathrm{W/cm^2}$ power density whereas, whereas standard $3700\,\mathrm{W}$ and $210\,\mathrm{mm}$ load diameter results in $10.7\,\mathrm{W/cm^2}$. The secondary' winding cable, number of turns and the compensation capacitors are chosen for prototyping. Capacitor connections are made via a printed circuit board (PCB) attached to the load and, in order to minimize the proximity losses caused by the magnetic field, a PCB litz-wire structure is adopted [22], [23].

The paper is organized as follows. The electrical model of the ICH system is developed in Section II. This section also includes the analysis of the inductive efficiency. The Section III presents the design considerations followed to implement the secondary inductor including the housing of the compensation capacitor. In order to validate both the model and design, several experimental results are shown in Section IV. Finally some conclusions are summarized in Section V. The efficiency analysis and compensation capacitor implementation are the biggest additions to the preceding conference paper [24], as well as expanded text and improved figures.
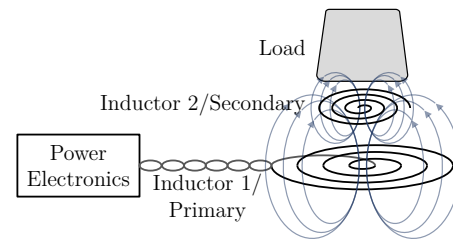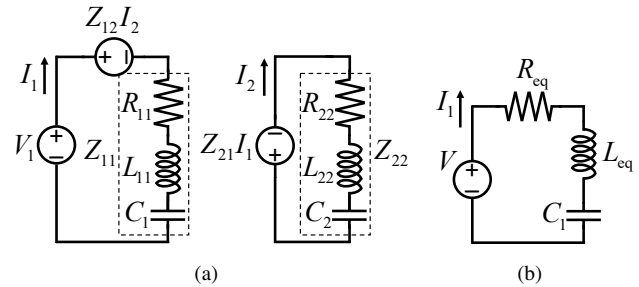
II. ICH SYSTEM ELECTRICAL MODEL

A. Inductor-load system electrical model

The implementation of the glassless IH cooker concept with a small receiver ICH system is depicted in Fig. 1. The primary inductor has $\varnothing_{w1,\mathrm{ext}} = 180\,\mathrm{mm}$ which corresponds to a standard size, not specific for small loads, in order to be compatible with loads of diameter ranging from 90 to $300\,\mathrm{mm}$. The primary inductor system is also standard and includes ferrite bars and shielding, which are placed beneath the kitchen worktop, while the $\varnothing_{\mathrm{load,ext}} = 90\,\mathrm{mm}$ load (represented as a moka pot) the secondary inductor and the compensation capacitors are placed above. The system is intended to work for a range of distances d_{w12} between 6 and $30\,\mathrm{mm}$. The secondary inductor and capacitor are housed together beneath the ferromagnetic load.

A diagram of the system is depicted in Fig. 2. The power electronics block represents a half-bridge series resonant inverter, which is also an standard in commercial products [25], [26]. Therefore, thanks to the ICH concept the arrangement of conventional IH apparatus can be used for glassless applications with small loads at high distance without deteriorating the performance.

The system electrical equivalent circuit is shown in Fig. 3 (a). This circuit consists of two inductively coupled circuits, each one corresponding to a winding, and the series compensation capacitors. Elements R_{ii} and L_{ii} represents the power dissipated and the stored magnetic energy when the ith inductor works on its own, respectively. The element Z_{12} represents the coupling impedance. In the case of IH applications this term is complex and therefore includes both real and imaginary components, i.e. $Z_{12} = R_{12} + j\omega L_{12}$. The imaginary part corresponds to the mutual inductance, whereas the resistive part accounts for the dissipative effect of the load, which is similar to the effect of a lossy core in a transformer. The coupling impedance reflects the fact that the

phase between the primary current and the secondary induced voltage is different from $\pi/2$ [27]. The circuit shown in Fig. 3 (a) can be also be expressed by the system of equations:

$$\begin{pmatrix} V \\ 0 \end{pmatrix} = \begin{pmatrix} Z_{11} & Z_{12} \\ Z_{21} & Z_{22} \end{pmatrix} \begin{pmatrix} I_1 \\ I_2 \end{pmatrix}, \tag{1}$$

where the diagonal elements include capacitors, and $V_2 = 0$ since the secondary inductor is not externally fed.

The elements R_{ii}, L_{ii} and Z_{ij} are obtained via finite element simulations with the COMSOL Multiphysics software. These elements also depend on the operating frequency. The equivalent impedance of the full system from the point of view of the inverter, Z_{eq}, can be defined as:

$$Z_{\text{eq}} = \frac{V}{I_1} = Z_{11} - \frac{Z_{12}^2}{Z_{22}}. \tag{2}$$

Z_{eq} includes resistive and inductive components, as well as the primary resonant capacitor:

$$Z_{\text{eq}} = R_{\text{eq}} + j\omega L_{\text{eq}} + \frac{1}{j\omega C_1} \tag{3}$$

The equivalent circuit is represented in Fig. 3 (b).

Some parameters of the primary inductor system are fixed due to it being an standard. Specifically, the number of turns of the primary is $n_{t,1} = 19$ and $C_1 = 800\,\text{nF}$. Conversely, $n_{t,2}$ and C_2 have to be chosen. For this reason, per turn simulations are carried out due to its interest in the design process. Considering the relation with per-turn impedance, the elements of the precedent equation can be written as follows:

$$Z_{\text{eq,p.t.}} = R_{\text{eq,p.t.}} + j\omega L_{\text{eq,p.t.}} + \frac{1}{j\omega C_{1,\text{p.t.}}}, \tag{4}$$

$$R_{\text{eq}} = n_{t,1}^2 R_{\text{eq,p.t.}}, \tag{5}$$

$$L_{\text{eq}} = n_{t,1}^2 L_{\text{eq,p.t.}}, \tag{6}$$

$$R_{\text{eq,p.t.}} = R_{11,\text{p.t.}} + \frac{2R_{12,\text{p.t.}}\omega L_{12,\text{p.t.}}\left(\omega L_{22,\text{p.t.}} - \frac{1}{\omega C_{2,\text{p.t.}}}\right)}{R_{22,\text{p.t.}}^2 + \left(\omega L_{22,\text{p.t.}} - \frac{1}{\omega C_{2,\text{p.t.}}}\right)^2} - \frac{\left(R_{12,\text{p.t.}}^2 - \omega^2 L_{12,\text{p.t.}}^2\right) R_{22,\text{p.t.}}}{R_{22,\text{p.t.}}^2 + \left(\omega L_{22,\text{p.t.}} - \frac{1}{\omega C_{2,\text{p.t.}}}\right)^2}, \tag{7}$$
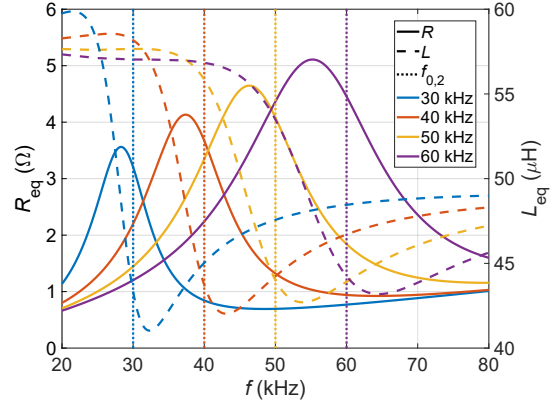

Fig. 4: Impedance extrema with changing secondary resonant frequency.

$$L_{\text{eq,p.t.}} = L_{11,\text{p.t.}} + \frac{2R_{12,\text{p.t.}}\omega L_{12,\text{p.t.}} R_{22,\text{p.t.}}}{\omega \left(R_{22,\text{p.t.}}^2 + \left(\omega L_{22,\text{p.t.}} - \frac{1}{\omega C_{2,\text{p.t.}}}\right)^2\right)} - \frac{\left(R_{12,\text{p.t.}}^2 - \omega^2 L_{12,\text{p.t.}}^2\right)\left(\omega L_{22,\text{p.t.}} - \frac{1}{\omega C_{2,\text{p.t.}}}\right)}{\omega \left(R_{22,\text{p.t.}}^2 + \left(\omega L_{22,\text{p.t.}} - \frac{1}{\omega C_{2,\text{p.t.}}}\right)^2\right)}, \tag{8}$$

$C_{1,\text{p.t.}}$ and $C_{2,\text{p.t.}}$ are mathematical *per-turn* capacitors that enable the relation:

$$X_{ii} = n_{t,i}^2 \left(\omega L_{ii,\text{p.t.}} - \frac{1}{\omega C_{i,\text{p.t.}}} \right) = n_{t,i}^2 X_{ii,\text{p.t.}} \tag{9}$$

where X_{ii} is the reactance of Z_{ii} and $X_{ii,\text{p.t.}}$ is the single-turn reactance.

As observed in (4)-(6), the total equivalent impedance only depends on $n_{t,1}$, whereas $n_{t,2}$, the number of turns of the passive inductor, is not part of these equations. This does not mean, however, that $n_{t,2}$, is meaningless, as it is a determining factor for I_2 and inductor/capacitor voltage, $V_{\text{ind},2} = -V_{\text{C},2}$. Moreover, according to (9), the reactance X_{22} depends on $n_{t,2}$. Therefore,

$$I_2 = -\frac{n_{t,1}}{n_{t,2}} \frac{Z_{12,\text{p.t.}}}{Z_{22,\text{p.t.}}} I_1, \tag{10}$$

$$V_{\text{C}2} = \frac{I_2}{j\omega C_2} = jn_{t,1}n_{t,2} \frac{Z_{12,\text{p.t.}}}{\omega C_{2,\text{p.t.}} Z_{22,\text{p.t.}}} I_1 \tag{11}$$

For a fixed value of $n_{t,1}$, I_2 is inversely proportional to $n_{t,2}$ and $V_{\text{ind},2}$, $V_{\text{C},2}$ are proportional to $n_{t,2}$.

The presence of multiple resonant tanks causes multiple resonant frequencies to exist:

$$\omega_{0,1} = \frac{1}{\sqrt{L_{11}C_1}} \tag{12}$$

$$\omega_{0,2} = \frac{1}{\sqrt{L_{22}C_2}} \tag{13}$$

$$\omega_{0,\text{eq}} = \frac{1}{\sqrt{L_{eq}C_1}} \qquad (14)$$

where $\omega_{0,1}$, $\omega_{0,2}$, $\omega_{0,\text{eq}}$ are the angular resonant frequencies for the primary inductor, secondary inductor and full equivalent system (i.e. the resonance frequency of the inverter's load) respectively.

To ensure low stress in the electronics and minimize power losses, the currents should be kept as low as possible, particularly at higher P demands, with $1500\,\text{W}$ maximum power. This can be achieved by a careful selection of C_2, to generate a maximum in R_{eq} and a minimum in L_{eq} near $\omega_{0,2}$, or equivalently, to achieve the maximum power factor. Fig. 4 shows the effect of ω and $f_{0,2}$ on the impedance fed by the inverter (7), (8). Near $f_{0,2}$, R_{eq} increases significantly up to a peak and then decreases, while L_{eq} drops significantly and then rises slowly. For each $f_{0,2}$, the R_{eq} peak occurs slightly below $f_{0,2}$, and the L_{eq} valley is placed slightly above $f_{0,2}$. The R_{eq} peak and L_{eq} valley produce a PF peak and sharp decreases at either side. Therefore, it is highly desirable to operate at or near $f_{0,2}$ to increase performance.

B. Model of winding losses and inductive efficiency

As it was above commented, the primary inductor is inherited from a commercial application in which litz wire is commonly used due to its superior performance with respect to unifilar cables, specially regarding the winding loss reduction. For this reason, this cable will be also used to design the secondary winding. The design of the secondary winding entails the selection of the wire, which comprises the calculation of $n_{t,2}$, the number of strands $n_{s,2}$, and the strand diameter $\varnothing_{s,2}$. The number of turns can be selected considering the expressions (10), (11) of the precedent section. However, the number and diameter of strands are rather selected according to an efficiency criterion.

Inductive efficiency can be defined as power delivered in the load P_{load} divided by the power supplied by the primary inverter. Neglecting the losses in capacitors, connectors and other auxiliary elements, this efficiency can be expressed as follows:

$$\eta = \frac{P_{\text{load}}}{P_{\text{load}} + P_{\text{win}} + P_{\text{fer}} + P_{\text{shd}}} \qquad (15)$$

where P_{win} represents the winding losses, P_{fer} are the ferrite losses, and P_{shd} are the aluminum shielding losses. Moreover, P_{win} comprises the losses in both primary and secondary windings and it also encapsulates the dc resistance, and the ac resistance effects, namely skin and proximity effects.

Efficiency can be modelled in terms of resistances whose value depends on the parameters and geometry of the system. This model can be very complex in ICH systems due to the coupling between primary and secondary, which is translated as coupled dissipative effects. However, the model can be simplified if the following assumptions are adopted:

- At the interest frequency range (20 to $75\,\text{kHz}$) ferrite and shielding losses are smaller than winding losses and therefore they can be neglected [28].
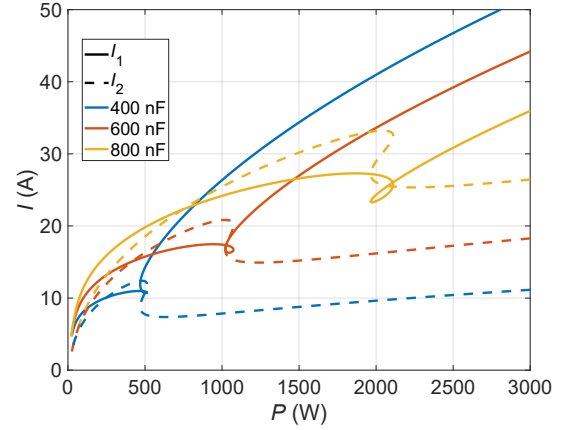

Fig. 5: Current variation with secondary capacitor.

- Primary and secondary windings only generate proximity losses in its own turns. Cross terms of proximity losses are also neglected [29].
- Copper litz wire with ideal structure (i.e. perfect transposition of strands) is considered. Consequently, all strands are equivalent [30].
- Skin and proximity effects in the litz wire at bundle level are neglected [31] and the magnetic field is not modified by the induced currents in the windings. Consequently, windings can be modelled as ideal current densities in FEA simulations.
- The diameter of strands is chosen smaller than the skin depth at the interest frequency range. Therefore, low frequency (LF) approximations for the skin and proximity ac-resistance factors can be used [32].

In these conditions, the expression (16) can be written as follows:

$$\eta = \frac{R_{\text{eq}}}{R_{\text{eq}} + R_{\text{dc},1} + R_{\text{prox},1} + R_{\text{dc},2} + R_{\text{prox},2}} \qquad (16)$$

where the dc resistance of the ith winding is:

$$R_{\text{dc},i} = \frac{1}{\sigma_{\text{Cu}}} \frac{n_{t,i}}{n_{s,i}} \frac{\text{MLT}_i}{\pi r_{s,i}^2} \qquad (17)$$

MLT being the mean length of the turn.

The proximity losses term $R_{\text{prox},i}$ depends on the squared modulus of the magnetic field generated by each inductor over its own conductors and the conductor's length, also bearing in mind that the field strongly depends on the position. The following expression captures the dependency of the proximity resistance with respect to the field for a specific winding geometry [23]:

$$\left\langle \left| \overline{\mathbf{H}}_{i,\text{p.t.}} \right|^2 \right\rangle = \frac{1}{S_{\text{coil},i}} \int_{V_{\text{coil},i}} \left| \overline{\mathbf{H}}_{i,\text{p.t.}} \right|^2 dv \qquad (18)$$

where $S_{\text{coil},i}$ is the coil cross-sectional area, $V_{\text{coil},i}$ is the coil volume, and $\overline{\mathbf{H}}_{i,\text{p.t.}}$ is the normalized amplitude of the field per unit of ampere and per turn, respectively. The expression 18 can be evaluated by means of per-turn FEA simulation. Considering this magnitude, the proximity resistance of the ith coil is:
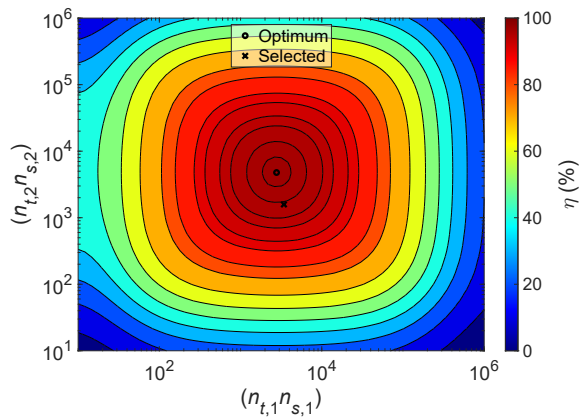
Fig. 6: Efficiency variation due to different $(n_{t,1}n_{s,1})$ and $(n_{t,2}n_{s,2})$ at $d_{w12} = 20\,\text{mm}$ at $d_{w12} = 20\,\text{mm}$.
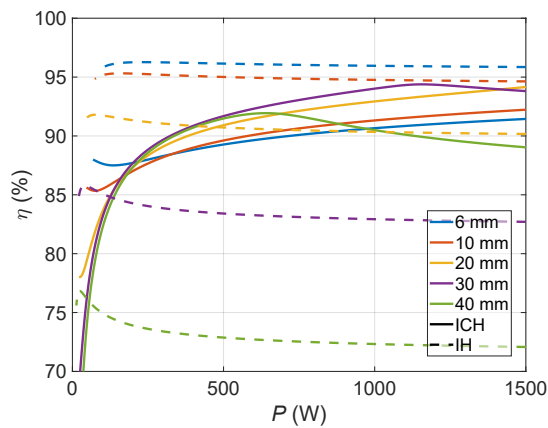

Fig. 7: Simulated efficiency of the full ICH system and primary only (IH).

TABLE I: Parameters of the designed ICH system.

Description	Symbol	Primary	Secondary	Units
Number of turns	$n_{t,i}$	19	22	[-]
Internal radius	$\varnothing_{wi,\text{int}}$	49	26	mm
External radius	$\varnothing_{wi,\text{ext}}$	180	90	mm
Cable type		Litz wire		
Number of strands	$n_{s,i}$	180	72	[-]
Strand diameter	$\varnothing_{s,i}$	200	200	μm
Compensation capacitor	C_i	800	750	nF

$$R_{\text{prox},i} = \frac{\pi}{\sigma_{\text{Cu}}} n_{s,i} n_{t,i}^3 \left(\frac{r_{s,i}}{\delta}\right)^4 \left\langle \left|\overline{\mathbf{H}}_{i,\text{p.t.}}\right|^2 \right\rangle \qquad (19)$$

where δ is the skin depth of the magnetic field in the copper at ω, $\delta = \sqrt{2/(\omega\sigma_{Cu}\mu_0)}$. According to expressions (5), (17) and (19) the efficiency depends on the number of turns and the number of strands of both inductors.

III. System analysis and design

A. Inductor-load system

This analysis aims at obtaining the value of C_2 and the secondary' number of turns $n_{t,2}$ and strands $n_{s,2}$. The simulated distances between windings, d_{w12}, range from 6 to 40 mm, so that the system could be used in IH applications with ceramic glass as well as in the glassless concept with a thick worktop.
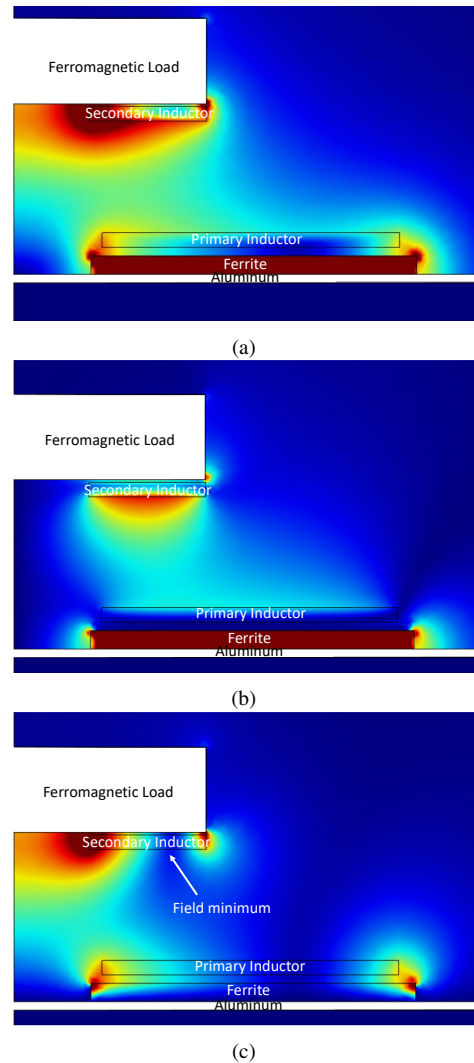

(a)

(b)

(c)

Fig. 8: 2D axysimmetric simulation of **B** field: (a) $|\mathbf{B}|$, (b) $|B_r|$, (c) $|B_z|$.
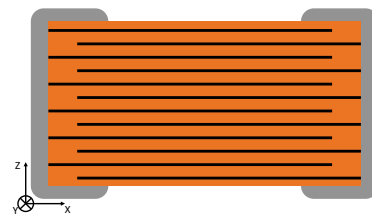

Fig. 9: Multilayer ceramic capacitor diagram

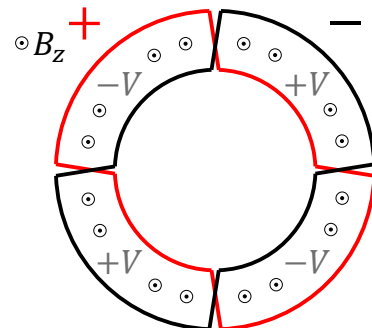Fig. 10: Voltage induction in twinned tracks.

This article has been accepted for publication in IEEE Transactions on Industry Applications. This is the author's version which has not been fully edited and content may change prior to final publication. Citation information: DOI 10.1109/TIA.2022.3193107

6

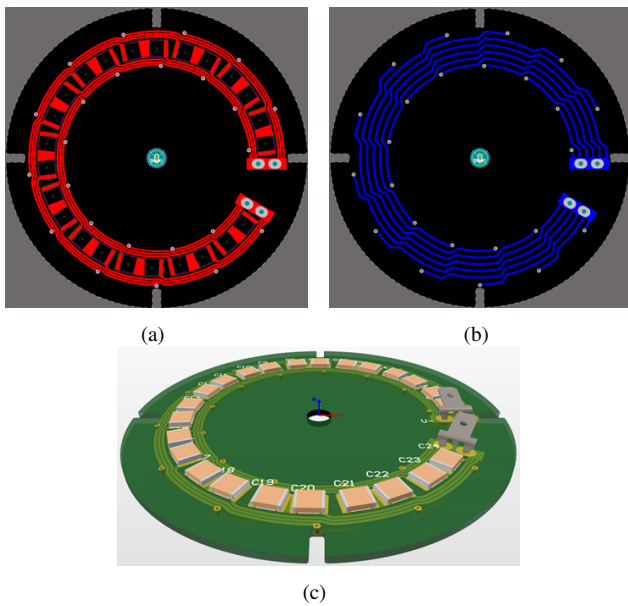

(a)   (b)

(c)

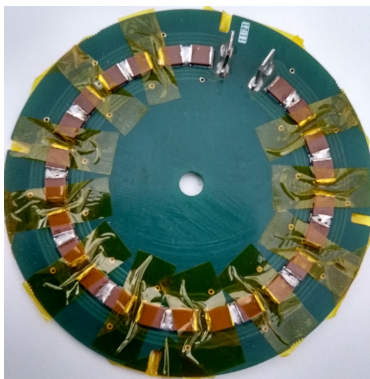Fig. 11: Individual PCB track routing: (a) top layer, (b) bottom layer, (c) PCB perspective.

Fig. 12: PCB individual track prototype (PCBLitz).

Fig. 5 depicts the dependence of I_1 and I_2 with C_2, and consequently $f_{0,2}$, for the $d_{w12} = 20\,\mathrm{mm}$ case where power is frequency controlled. As C_2 increases, $f_{0,2}$ decreases, moving the PF peak to higher power levels. Thus, current can be minimized for a particular power level, improving near points but penalizing those further away. The same comparison has been carried out for distances between 6 and $40\,\mathrm{mm}$, and the $750\,\mathrm{nF}$ option for C_2 in conjunction with $n_{t,2} = 22$ is the most beneficial secondary capacitor to minimize current in most of the considered situations.

Fig. 6 shows simulated η with sweeping values of $(n_{t,1}n_{s,1})$ and $(n_{t,2}n_{s,2})$ and highlighted optimum and selected values. The primary inductor maintains the $n_{s,1} = 180$, $\varnothing_{s,1} = 200\,\mu\mathrm{m}$ from standard appliances. Due to space restrictions the secondary inductor can only house $n_{s,2} = 72$ strands out of the optimum 217. However, the effect in the efficiency is less than 1%.

The simulated η of the chosen design are plotted in Fig. 7, comparing the IH situation where only the primary inductor is active and the full ICH system. The addition of the secondary inductor decreases overall η at low d_{w12} due to the additional
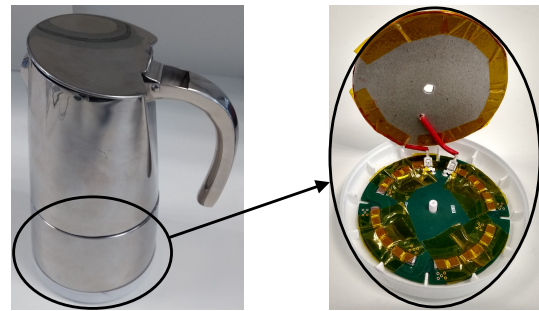

Fig. 13: Moka pot with housing attached on the left and open housing with capacitor PCB and secondary winding on the right.
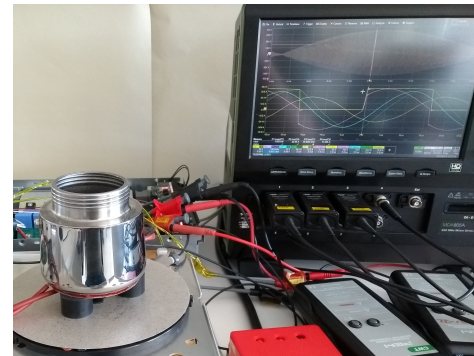

Fig. 14: Experimental setup.

passive components and particularly at low power, but clearly improves η above $10\,\mathrm{mm}$ distances, where conventional IH η drops quickly due to the small load resistance in proportion to winding and shielding losses [7].

The main parameters of the designed system are collected in Table I.

B. Capacitor location and orientation

There is not much space to integrate the compensation capacitors with moka pots. In any case, it is preferable to include all electronics in the same compartment and prevent multiple interconnected pieces that attach to the load. Moreover, in ICH, the magnetic field must reach the ferromagnetic load, and shielding is not an option.

FEA simulations show that $|\mathbf{B}|$, the norm of the $\mathbf{B}$ field is strong near the secondary inductor, represented in Fig. 8 (a). However, its distribution is not uniform along the three spatial directions. Magnetic flux in the azimuthal direction, B_φ, is zero due to the axial symmetry, the flux modulus in the radial direction, $|B_r|$, is represented in Fig. 8 (b), and the flux modulus in the vertical direction, $|B_z|$, is represented in Fig. 8 (c).

There is a space at $3/4 r_{w2,\mathrm{ext}}$ where B_z is low, while B_r is quite strong and stable. In that position, the effects of B_z are minimal and so it becomes the optimal position to place components. Moreover, objects that have a low profile along one direction can be aligned with the radial direction to minimize induced voltage in said direction, while the field strength in the other directions is not strong enough to cause significant effects.
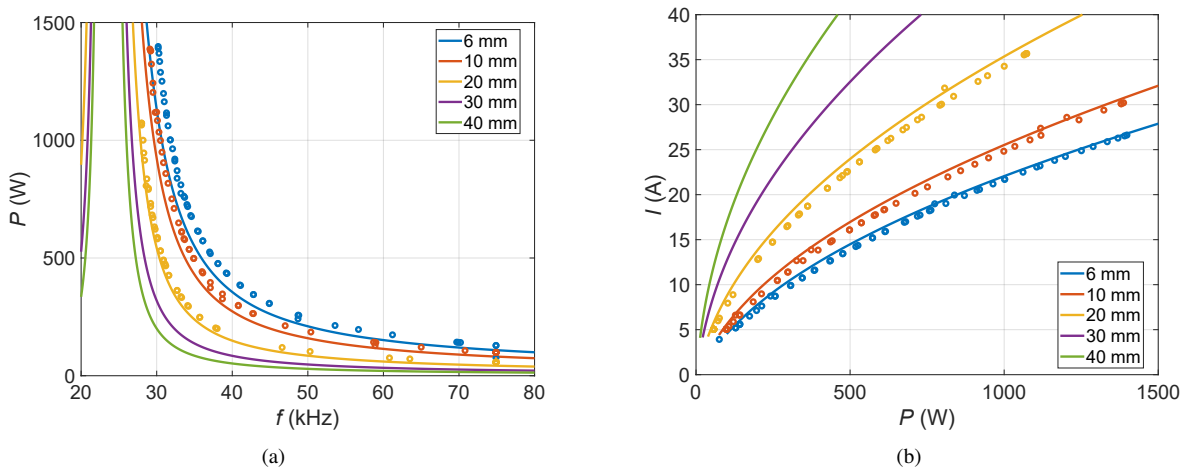
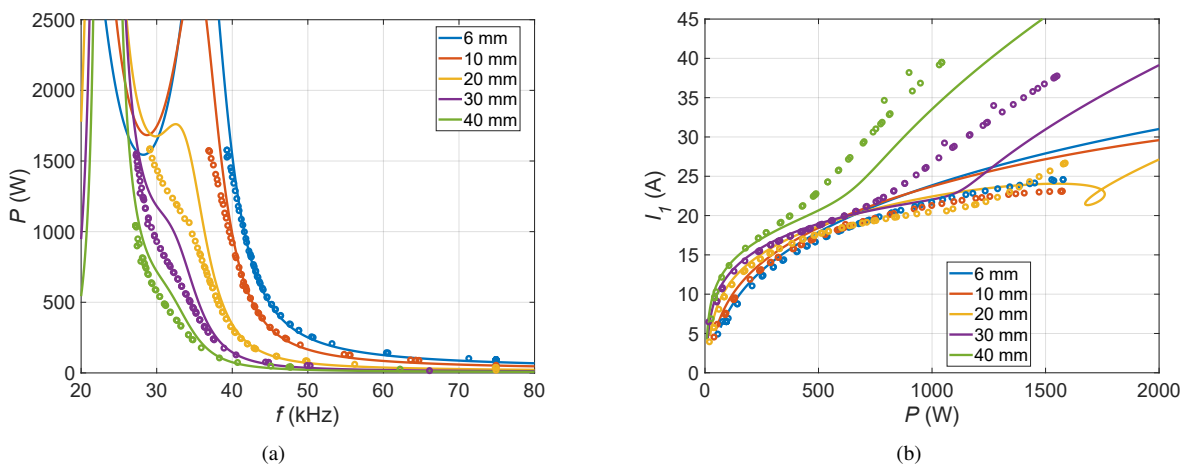Fig. 15: Primary inductor only (IH) measurements at $d_{\text{load}} = 20 \, \text{mm}$ of (a) P and (b) I.

Fig. 16: Full system (ICH) measurements of (a) P and (b) I.

Surface mounted devices and electronic boards can benefit the most from this kind of magnetic field distribution, since these devices are generally quite thin, as are the copper tracks of the boards they are mounted on.

In the case of multi-layer ceramic capacitors (MLCC), whose diagram is shown in Fig. 9, they have the biggest metallic surface in the Z direction. Due to the electrodes, they have some surface area in the X direction. They project the least surface in the Y direction, because of the thinner part of the terminals, and the thin cross section of the electrodes.

Proximity losses generated in the capacitors increase considerably with the metallic cross-section facing the magnetic field. As the biggest cross-section, the Z plane must be placed in a low flux direction. Therefore, the surface mounted capacitors align their local Z direction with the B_z field, in the location where the vertical flux is minimal. Additionally, it is preferable to orient the local Y direction with the B_r direction, combining the minimum cross-section with the maximum field and avoid more losses.

C. Induced voltage, track twinning and track routing

To fully cancel the effect of B_z, the cables or PCB tracks carrying different voltages can be twinned to simultaneously balance currents, reduce the intersecting area and invert the polarity of each successive loop, minimizing induced voltage in most cases and completely cancelling it in geometries with axial symmetry, as shown in Fig. 10.

Since the PCB tracks may be the most affected part of the system, a reduction in proximity losses can also significantly reduce the temperature increment in the tracks. A possible solution is the separation of the main PCB track into individual thinner tracks for each of the parallel capacitors [23]. An application example of the adopted guidelines are shown in Fig. 11. Moreover, Fig. 12 shows a picture of the prototype with the PCB-litz wire implementation, shortened for convenience as PCBLitz.

The prototype was implemented in a small housing with the secondary inductor, as shown in Fig. 13 on the right, and then fitted to the moka pot shown on the left, highlighting the ICH prototype's small size and unobtrusive look.

IV. Experimental results

A. Electrical measurements

The full system has been tested delivering P up to $1500 \, \text{W}$ at the simulated distances with frequency control and a

This article has been accepted for publication in IEEE Transactions on Industry Applications. This is the author's version which has not been fully edited and content may change prior to final publication. Citation information: DOI 10.1109/TIA.2022.3193107

8

TABLE II: Parameter comparison between IH with the primary inductor only and the full ICH system (simulations)

Distance (mm)	Primary only			Full ICH system		
	$P_{\max}$ (W) @ < 40 A	I (A) @ < 1500 W	η (%) @ < 1500 W	$P_{\max}$ (W) @ < 40 A	I_1 (A) @ < 1500 W	η (%) @ < 1500 W
6 mm	2840	28	95.8	3400	28	91.4
10 mm	2250	32	94.6	3900	27	92.2
20 mm	1240	44	90.1	3200	24	94.2
30 mm	730	59	82.7	2080	31	93.8
40 mm	460	74	72.0	1250	45	89.0

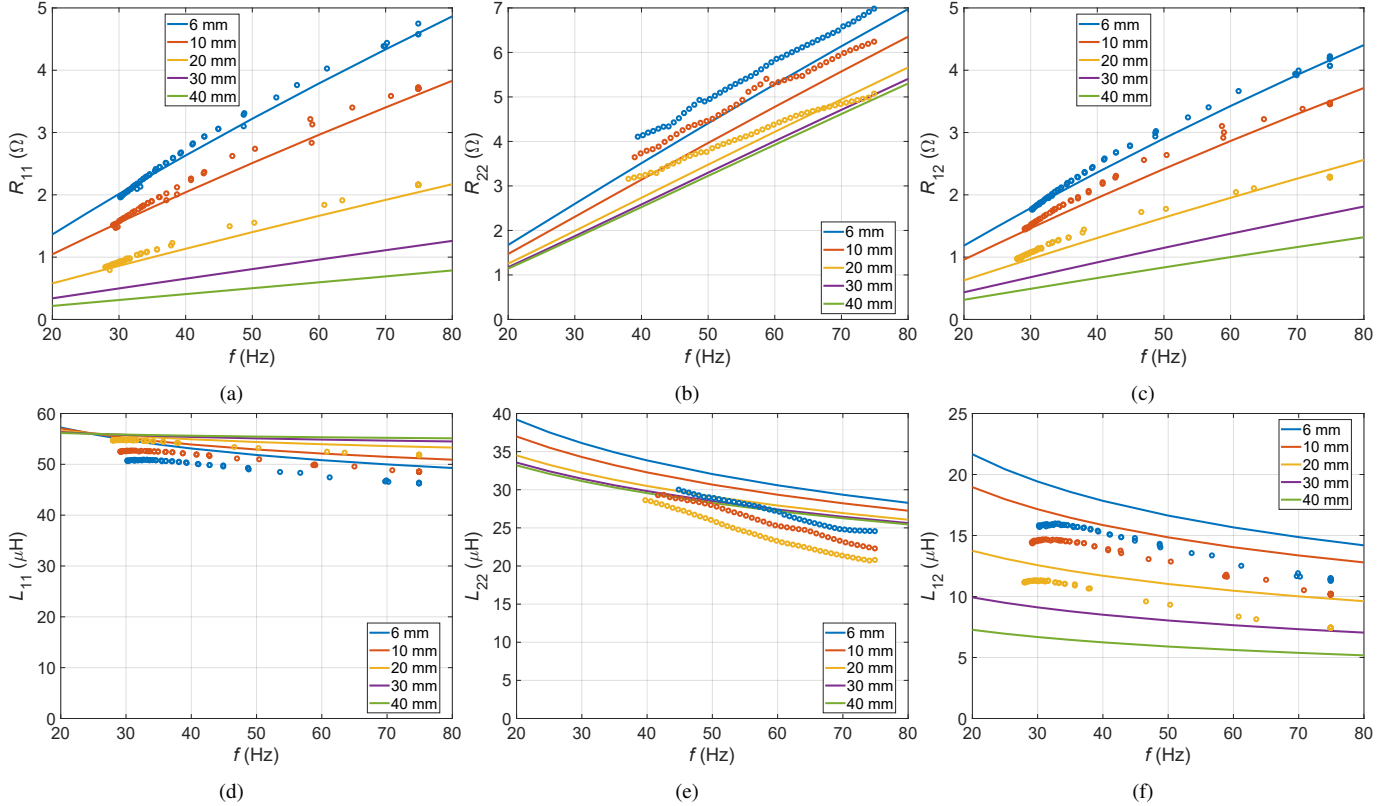
Fig. 17: Simulated and calculated winding impedance: (a) R_{11} (b) R_{22} (c) R_{12} (d) L_{11} (e) L_{22} (f) L_{12}

$\varnothing_{w1,\text{ext}} = 180\,\text{mm}$ commercial cooktop inductor. Wave measurements of inverter voltage, inductor voltages and currents have been taken with an oscilloscope. Measurements with the secondary inductor in open circuit have also been taken to compare results between the IH system with the primary inductor only and the full ICH system. The additional measurements are also used to calculate the elements of the impedance matrix.

Fig. 14 shows the experimental setup, where the primary and secondary inductors have been separated $d_{w12} = 20\,\text{mm}$ with measured disks of PPS. Simulated and measured values of P and I_1 for the IH primary inductor only case in Fig. 15 and for the full ICH system in Fig. 16. The measured values generally agree with the simulations, and the system behaves as expected. The figures and Table II confirm that the active secondary inductor manages to reduce I_1 for all cases, except low P at low d_{w12}.

Furthermore, the system's impedance has been calculated from the measurements of both the IH and the ICH case. The impedances that are calculated directly from the measured waveforms are Z_{eq} from the full ICH system, Z_{11} and Z_{12} from the IH system with the primary inductor only. Z_{22} is calculated indirectly as:

$$Z_{22} = \frac{Z_{12}^2}{Z_{11} - Z_{eq}}. \tag{20}$$

The individual winding impedances are shown in Fig. 17, where primary impedance and R_{12} matches very well, L_{12} and secondary impedance are slightly off. As R_{22} and L_{22} are obtained indirectly, the result is satisfactory. The equivalent impedance is shown in Fig. 18, where both R_{eq} and L_{eq} match fairly well except at the R_{eq} peak and the L_{eq} valley, due to the overestimation in the L_{12} simulation.

B. Thermal measurements

Temperature measurements were taken with a thermographic camera and several thermocouples in different positions. Moreover, two complementary configurations have been considered for measurements. In the first configuration the
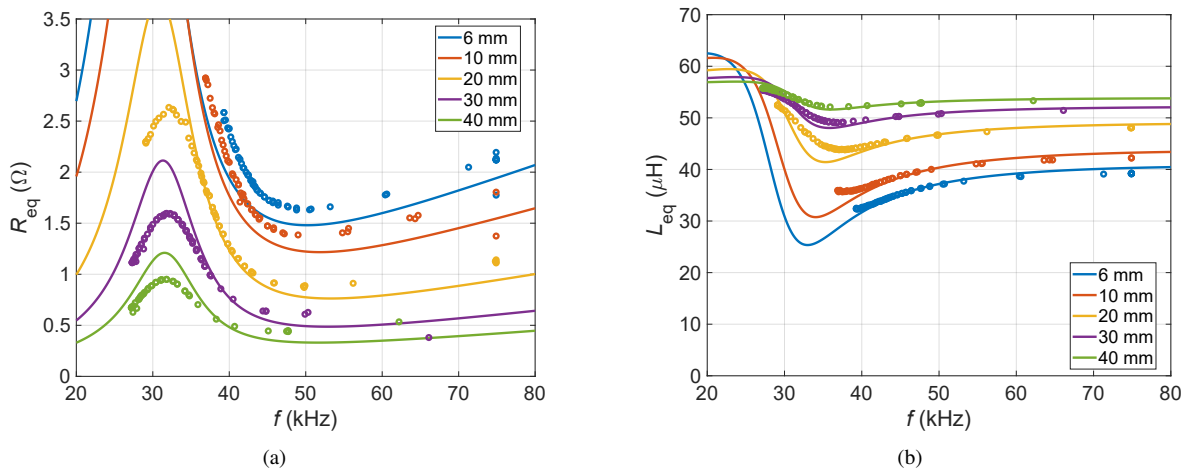
Fig. 18: Simulated and calculated impedance: (a) R_{eq} (b) L_{eq}
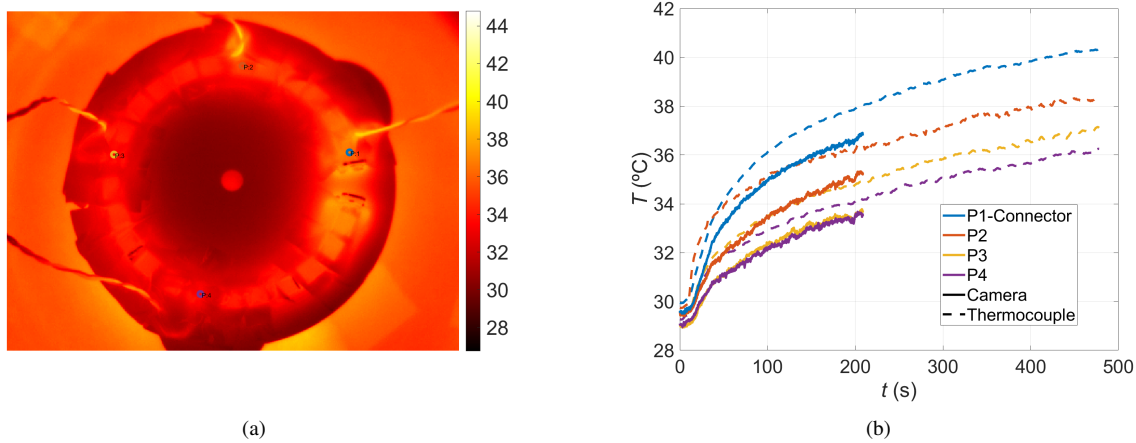

Fig. 19: PCBLitz under magnetic field: (a) thermographic image and (b) temperature increment.

ferromagnetic load is not present and, therefore, both the PCB and the capacitors are in a strong magnetic field. The second configuration corresponds to the whole system and the magnetic field in the PCB is lesser than in the previous case (due to the currents induced in the moka) but the PCB temperature is affected by the moka' temperature.

Fig. 19 shows a thermal image of the PCBLitz prototype and the measured temperatures with the camera and thermocouples of the marked points when a strong magnetic field is applied. In this case, after 500 s the temperature increment is 10 °C at most. This temperature increase is due to proximity losses in both tracks and capacitors.

Fig. 20 shows the PCBLitz temperature increment with the full system depicted in Fig. 13 operating at 500 W. The temperature is low in the worst-case capacitor, the one closest to the connector, and the rest have much lower temperature. The measurements show that the PCBLitz prototype could withstand the temperatures caused by normal operation.

V. CONCLUSION

Conventional IH systems have trouble with detection and heating of really small loads, especially when the distance between the inductor coil and the load is high. The simulations
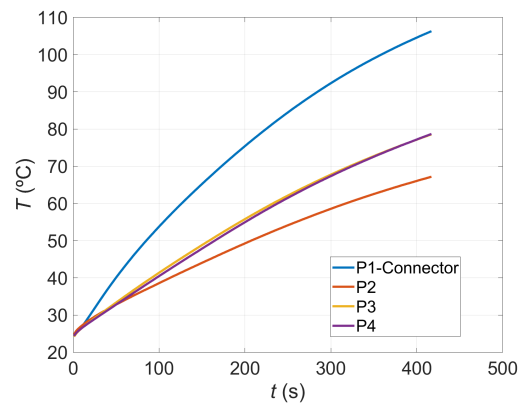

Fig. 20: Temperature increment in PCBLitz due to strong magnetic field, circulating current and thermal insulation.

and experimental results show that small loads can be adapted successfully with ICH systems, delivering much more power than conventional systems with adequate power factor and efficiency. Additionally, the resonant capacitors can be housed under the load without adverse effects from the magnetic fields, as confirmed by the thermal measurements.

The actions to prevent damage and interference to the

capacitors, ordered from more to less effective are:

- *Individual PCB track routing:* minimizes proximity losses in capacitor tracks.
- *Orientation of biggest capacitor metallic surface area with small magnetic flux:* significantly decreases heating in the capacitors.
- *Twinning tracks:* Reduces induced voltage in the resonant tank.
- *Orientation of the second biggest capacitor metallic surface area with small magnetic flux:* decreases heating in the capacitors.

Thermal and electric measurements show that with a few improvements, the secondary winding and resonant capacitors can be housed together and be attached beneath the ferromagnetic load.

REFERENCES

[1] J. Acero, J. M. Burdio, L. A. Barragan, D. Navarro, R. Alonso, J. García, F. Monterde, P. Hernandez, S. Llorente, and I. Garde, "Domestic induction appliances," *IEEE Industry Applications Magazine*, vol. 16, no. 2, pp. 39–47, Mar. 2010.

[2] O. Lucía, P. Maussion, E. J. Dede, and J. M. Burdío, "Induction heating technology and its applications: Past developments, current technology, and future challenges," *IEEE Transactions on Industrial Electronics*, vol. 61, no. 5, pp. 2509–2520, May 2014.

[3] L. Meng, K. W. E. Cheng, and K. W. Chan, "Systematic approach to high-power and energy-efficient industrial induction cooker system: Circuit design, control strategy, and prototype evaluation," *IEEE Trans. Power Electron.*, vol. 26, pp. 3754–3765, 2011.

[4] T. Mishima and M. Nakaoka, "A load-power adaptive dual pulse modulated current phasor-controlled zvs high-frequency resonant inverter for induction heating applications," *IEEE Trans. Power Electron.*, vol. 29, pp. 3864–3880, 2014.

[5] H. N. Pham, H. Fujita, K. Ozaki, and N. Uchida, "Estimating method of heat distribution using 3-d resistance matrix for zone-control induction heating systems," vol. 27, pp. 3374–3382, 2012.

[6] L. Wu, B. Zhang, Y. Jiang, and J. Zhou, "A robust parity-time-symmetric wpt system with extended constant-power range for cordless kitchen appliances," *IEEE Trans. Ind. Appl.*, early access 2021.

[7] E. Plumed, J. Acero, I. Lope, and J. M. Burdío, "Design methodology of high performance domestic induction heating systems under worktop," *IET Power Electronics*, vol. 13, no. 2, pp. 300–306, 2020.

[8] F. Sanz, C. Sagues, and S. Llorente, "Power distribution in coupled multiple-coilinductors for induction heating appliances," *IEEE Trans. Ind. Appl.*, vol. 52, no. 3, pp. 2537–2544, May 2016.

[9] J. Serrano, I. Lope, J. A. C. Carretero, J. M. Burdío, and R. Alonso, "Design and optimization of small inductors on extra-thin pcb for flexible cooking surfaces," *IEEE Trans. Ind. Appl.*, vol. 53, pp. 371–379, Jan. 2017.

[10] F. Sanz, C. Sagues, and S. Llorente, "Induction heating appliance with a mobile double-coil inductor," *IEEE Trans. Ind. Appl.*, vol. 51, pp. 1945–1952, 5 2015.

[11] W. Han, K. T. Chau, and Z. Zhang, "Flexible induction heating using magnetic resonant coupling," *IEEE Transactions on Industrial Electronics*, vol. 64, no. 3, pp. 1982–1992, Mar. 2017.

[12] E. Plumed, I. Lope, and J. Acero, "Induction heating adaptation of a different-sized load with matching secondary inductor to achieve uniform heating and enhance vertical displacement," *IEEE Transactions on Power Electronics*, vol. 36, no. 6, pp. 6929–6942, 2021.

[13] G. A. Covic and J. T. Boys, "Inductive power transfer," *Proc. IEEE*, vol. 101, no. 6, pp. 1276–1289, Jun. 2013.

[14] J. Garnica, R. A. Chinga, and J. Lin, "Wireless power transmission: From far field to near field," *Proceedings of the IEEE*, vol. 101, no. 6, pp. 1321–1331, Jun. 2013.

[15] J. Huang, Y. Zhou, Z. Ning, and H. Gharavi, "Wireless power transfer and energy harvesting: Current status and future prospects," *IEEE Wireless Communications*, vol. 26, no. 4, pp. 163–169, Aug. 2019.

[16] R. C. M. Gomes, M. A. Vitorino, D. A. Acevedo-Bueno, and M. B. de Rossiter Corrêa, "Multiphase resonant inverter with coupled coils for ac-ac induction heating application," vol. 56, pp. 551–560, 2020.

[17] W. Han, K. T. Chau, C. Jiang, and W. Liu, "All-metal domestic induction heating using single-frequency double-layer coils," *IEEE Transactions on Magnetics*, vol. 54, no. 11, pp. 1–5, Nov. 2018.

[18] E. Plumed, I. Lope, J. Acero, and J. M. Burdío, "Design of a three inductor system with one externally fed for an inductively coupled heating application," in *Proc. IECON 2019 - 45th Annual Conf. of the IEEE Industrial Electronics Society*, vol. 1, Oct. 2019, pp. 5070–5074.

[19] J. Egalon, S. Caux, P. Maussion, M. Souley, and O. Pateau, "Multiphase system for metal disc induction heating: Modeling and rms current control," *IEEE Trans. Ind. Appl.*, vol. 48, no. 5, pp. 1692–1699, 2012.

[20] J. Acero, I. Lope, J. Burdio, C. Carretero, and R. Alonso, "Performance evaluation of graphite thin slabs for induction heating domestic applications," *IEEE Trans. Ind. Appl.*, vol. 3, no. 51, pp. 2398–2404, May 2015.

[21] S. Saeed, J. Garcia, M. S. Perdigão, V. S. Costa, B. Baptista, and A. M. S. Mendes, "Improved inductance calculation in variable power inductors by adjustment of the reluctance model through magnetic path analysis," *IEEE Trans. Ind. Appl.*, vol. 2, no. 57, pp. 1572–1587, Mar. 2021.

[22] S. Cove and M. Ordonez, "Wireless-power-transfer planar spiral winding design applying track width ratio," *IEEE Trans. Ind. Appl.*, vol. 51, pp. 2423–2433, 5 2015.

[23] I. Lope, J. Acero, J. Burdío, C. Carretero, and R. Alonso, "Design and implementation of pcb inductors with litz-wire structure for conventional-size large-signal domestic induction heating applications," *IEEE Transactions on Industry Applications*, vol. 51, no. 3, pp. 2434–2442, May 2015.

[24] E. Plumed, I. Lope, J. Acero, and J. M. Burdío, "Domestic induction heating system with standard primary inductor for reduced-size and high distance cookware," in *IEEE Applied Power Electronics Conf. and Expo. (APEC) 2021*, 2021, pp. 2842–2847.

[25] A. Domínguez, , L. Barragan, A. Otín, D. Navarro, and D. Puyal, "Inverse-based power control in domestic induction heating applications," *IEEE Trans. Ind. Electron.*, vol. 61, no. 5, pp. 2612–2621, May 2014.

[26] J. Villa, D. Navarro, A. Dominguez, J. I. Artigas, and L. A. Barragan, "Vessel recognition in induction heating appliances—a deep-learning approach," vol. 9, pp. 16 053–16 061, 2021.

[27] C. Carretero, J. Acero, R. Alonso, and J. Burdio, "Normal-mode decomposition of surface power distribution in multiple-coil induction heating systems," *IEEE Trans. Magn.*, vol. 52, no. 2, pp. 1–8, Feb. 2016.

[28] J. Acero, R. Alonso, L. A. Barragán, and J. M. Burdío, "Modeling of planar spiral inductors between two multilayer media for induction heating applications," *IEEE Trans. Magn.*, vol. 42, pp. 3719–3729, 11 2006.

[29] C. Carretero, "Coupling power losses in inductive power transfer systems with litz-wire coils," *IEEE Trans. Ind. Electron.*, vol. 64, no. 6, pp. 4474–4482, Jun. 2017.

[30] J. Acero, R. Alonso, J. M. Burdío, L. A. Barragán, and D. Puyal, "Frequency-dependent resistance in litz-wire planar windings for domestic induction heating appliances," *IEEE Trans. Power Electron.*, vol. 21, pp. 856–866, 7 2006.

[31] K. Umetani, S. Kawahara, J. Acero, H. Sarnago, O. Lucia, and E. Hiraki, "Analytical formulation of copper loss of litz wire with multiple levels of twisting using measurable parameters," *IEEE Trans. Ind. Appl.*, vol. 57, pp. 2407–2420, 5 2021.

[32] C. Carretero, J. Acero, and R. Alonso, "TM-TE decomposition of power losses in multi-stranded litz-wires used in electronic devices," *Progress In Electromagnetics Research*, vol. 123, pp. 83–103, 2012. [Online]. Available: http://www.jpier.org/PIER/pier.php?paper=11091909